Chemical Engineering Journal 527 (2026) 171664

Contents lists available at ScienceDirect

Chemical Engineering Journal

journal homepage: www.elsevier.com/locate/cej

Plant vesicle-MOF hybrid gel triggers metabolic and macrophage reprogramming to boost colorectal cancer immunotherapy

Ling Weng [a,b,1], Miao Wang [c,1], Yumeng Zhang [a,1], Ruixiang Xu [a], Min Zhao [a,*], Chunjie Zhao [a,*], Yihe Huang [d,**]

[a] School of Pharmacy, Shenyang Pharmaceutical University, Wenhua Road 103, Shenyang, Liaoning Province, China
[b] Affiliated Hospital of Integrated Traditional Chinese and Western Medicine, Nanjing University of Chinese Medicine, Nanjing, China
[c] School of Life Science and Biopharmaceutics, Shenyang Pharmaceutical University, Wenhua Road 103, Shenyang, Liaoning, China
[d] School of Public Health, Shenyang Medical College, Huanghe North Street 146, Shenyang, Liaoning Province, China

ARTICLE INFO

Keywords:
Extracellular vesicles
Metal-organic Framework
Hyaluronic acid hydrogel
Photodynamic therapy
Colorectal cancer

ABSTRACT

The treatment of colorectal cancer (CRC) is limited by inefficient drug delivery, immunosuppression of the tumor micro-environment (TME) and neutralization of reactive oxygen species (ROS) by the antioxidant system. In this study, a biomimetic nanoplatform (ANPs+MOFs@HA) was designed to achieve photodynamic-chemical synergistic therapy and immune micro-environment remodeling by integrating American ginseng-derived extracellular vesicles (ANPs), copper-based metal-organic frameworks (Cu-MOFs) and hyaluronic acid (HA) hydrogels. The small-sized Cu-MOFs encapsulated by ANPs significantly enhanced the tumor penetration ability and enhanced the targeting of CD44 high-expressing colorectal cancer cells by HA modification. In vitro experiments demonstrated that ANPs+MOFs@HA upon near-infrared light irradiation, efficiently generated ROS, activated the TNF-α signaling pathway and induced a shift in macrophage polarization toward a pro-inflammatory state, characterised by increased M1 markers. In vitro experiments demonstrated that upon near-infrared light irradiation, ANPs+MOFs@HA efficiently generated ROS and activated the TNF-α signaling pathway, whereas the HA hydrogel matrix served to prolong the local retention of the elicited immunomodulatory factors. In a CT26 mouse model, ANPs+MOFs@HA received 650 nm laser irradiation (100 mW/cm^2, 20 min) at 4 h post-administration significantly inhibited tumor growth, upregulated the proportion of CD86$^+$ M1 macrophages within the tumor and reduced the expression of the immune-suppressive factors IL-10 and TGF-β. Histological and metabolomic analyses further revealed that the platform synergistically reversed the immunosuppressive micro-environment through metabolic reprogramming and NF-κB pathway inhibition without significant organ toxicity. This study provides a new idea for precision immunotherapy strategy based on the synergy of natural vesicles and synthetic materials, which has a broad potential for clinical application.

1. Introduction

Colorectal cancer (CRC) remains a formidable global health challenge as the third most prevalent malignancy [1,2], with post-treatment recurrence and distant metastasis severely compromising clinical outcomes despite therapeutic advancements [3]. While immune checkpoint inhibitors have revolutionized cancer immunotherapy for select patient subgroups [4], their efficacy in CRC is fundamentally constrained by the immunosuppressive tumor microenvironment (TME) [5,6], systemic drug resistance mechanisms [7] and inadequate tumor-specific targeting. These limitations underscore the urgent need for innovative therapeutic strategies that simultaneously address multiple dimensions of tumor biology.

Photodynamic therapy (PDT) presents a promising avenue through its dual capacity for localized tumor ablation via photosensitizer-derived reactive oxygen species (ROS) [8,9] and systemic immune activation via immunogenic cell death [10,11]. However, conventional PDT efficacy is critically limited by rapid antioxidant-mediated ROS scavenging and

* Corresponding authors at: School of Pharmacy, Shenyang Pharmaceutical University, No. 103 Wenhua Road, Shenyang, 110016, Liaoning, China.
** Corresponding author.
E-mail addresses: 101040224@syphu.edu.cn (M. Zhao), lab433@163.com (C. Zhao), huangyihe@symc.edu.cn (Y. Huang).
[1] Ling Weng, Miao Wang and Yumeng Zhang contributed equally.

https://doi.org/10.1016/j.cej.2025.171664
Received 20 August 2025; Received in revised form 15 November 2025; Accepted 6 December 2025
Available online 8 December 2025

suboptimal tissue penetration of existing photosensitizers [12]. The emergence of metal-organic frameworks (MOFs) as next-generation nanoplatforms offers solutions through their engineered porosity [13–15] and catalytic functionalities. Notably, Cu-MOFs demonstrate enhanced ROS generation [16] while simultaneously releasing bioactive Cu^{2+} ions capable of modulating critical immune pathways [17] through Cu^{2+} release [18]. Nevertheless, inherent rigidity and rapid systemic clearance of conventional MOFs restrict their tumor penetration and therapeutic bioavailability.

In recent years, plant-derived extracellular vesicles (PNPs) [19] have become a research hotspot in the field of drug delivery [20] due to their natural phospholipids bilayer structure [21], low immunogenicity and excellent biocompatibility [22]. ANPs have been shown to efficiently load hydrophobic drugs and enhance cellular uptake via membrane fusion mechanism [23], and their surface active components may also be involved in immunology-modulation. In addition, HA can be constructed as a targeted delivery system by virtue of its specific binding ability to the CD44 receptor [24], while its hydrogel form can prolong the retention time of drugs at the lesion site [25].

Integrating these advances, we engineer a multimodal biomimetic nanoplatform (ANPs+MOFs@HA) to directly address the aforementioned challenges in CRC therapy. Specifically, to solve the challenge of

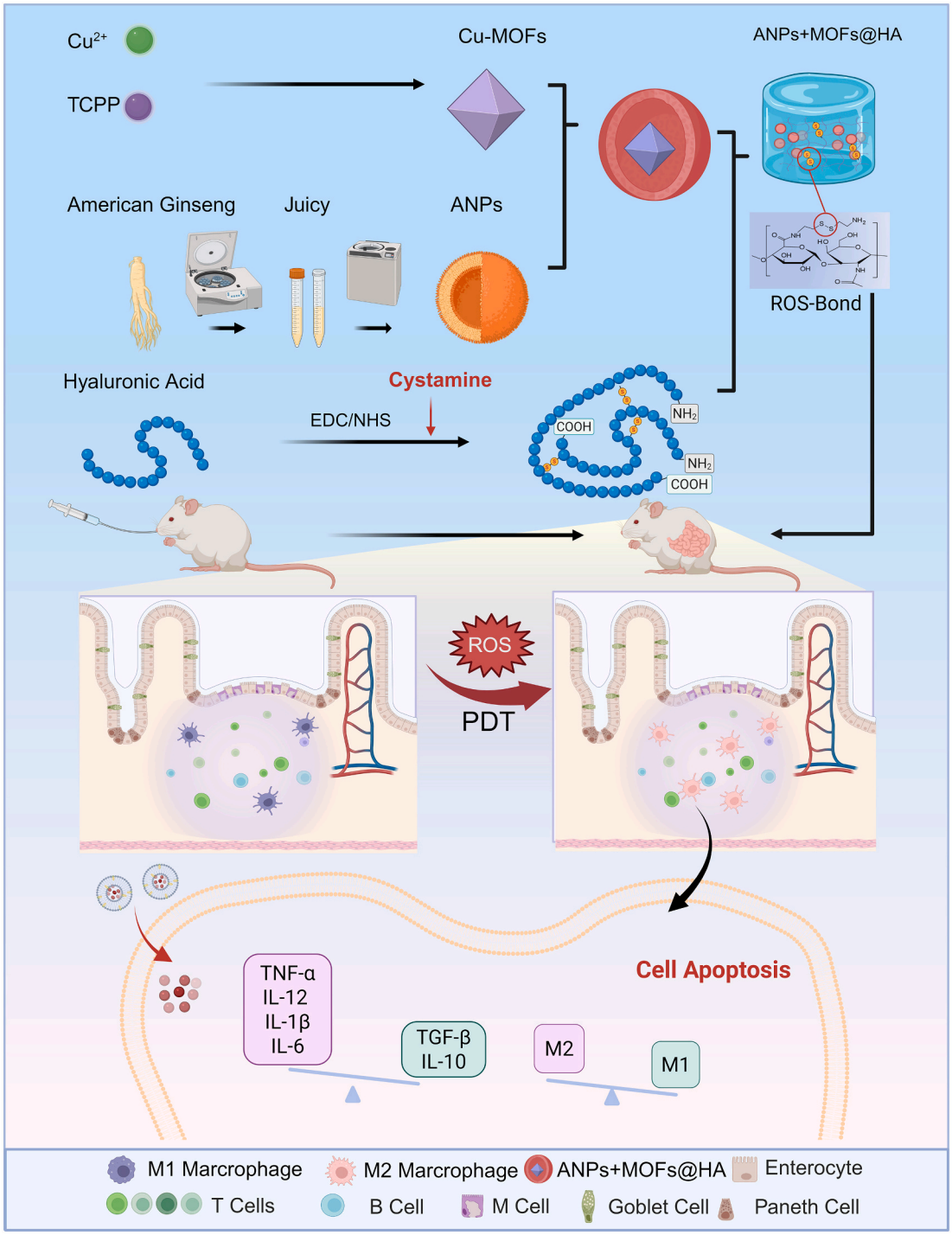

Scheme 1. Illustration of synthesis of ANPs+MOFs@HA for CRC therapy.

inefficient drug delivery and poor tumor penetration, we designed tumor-penetrating ultra-small Cu-MOFs nanodots encapsulated within PNPs-derived natural delivery vehicles for enhanced biocompatibility and cellular uptake [26]. To overcome the limitation of non-specific targeting and rapid clearance, we introduced HA-mediated active tumor targeting and pharmacokinetic optimization. Finally, to counter the immunosuppressive TME and the neutralization of ROS by the antioxidant system, our platform leverages Cu^{2+}-driven TME remodeling through macrophage M1 polarization and localized ROS amplification. This hierarchical design not only strategically overcomes the antioxidant defense barrier but also converts traditionally inert drug carriers into immunologically active therapeutic agents. Through

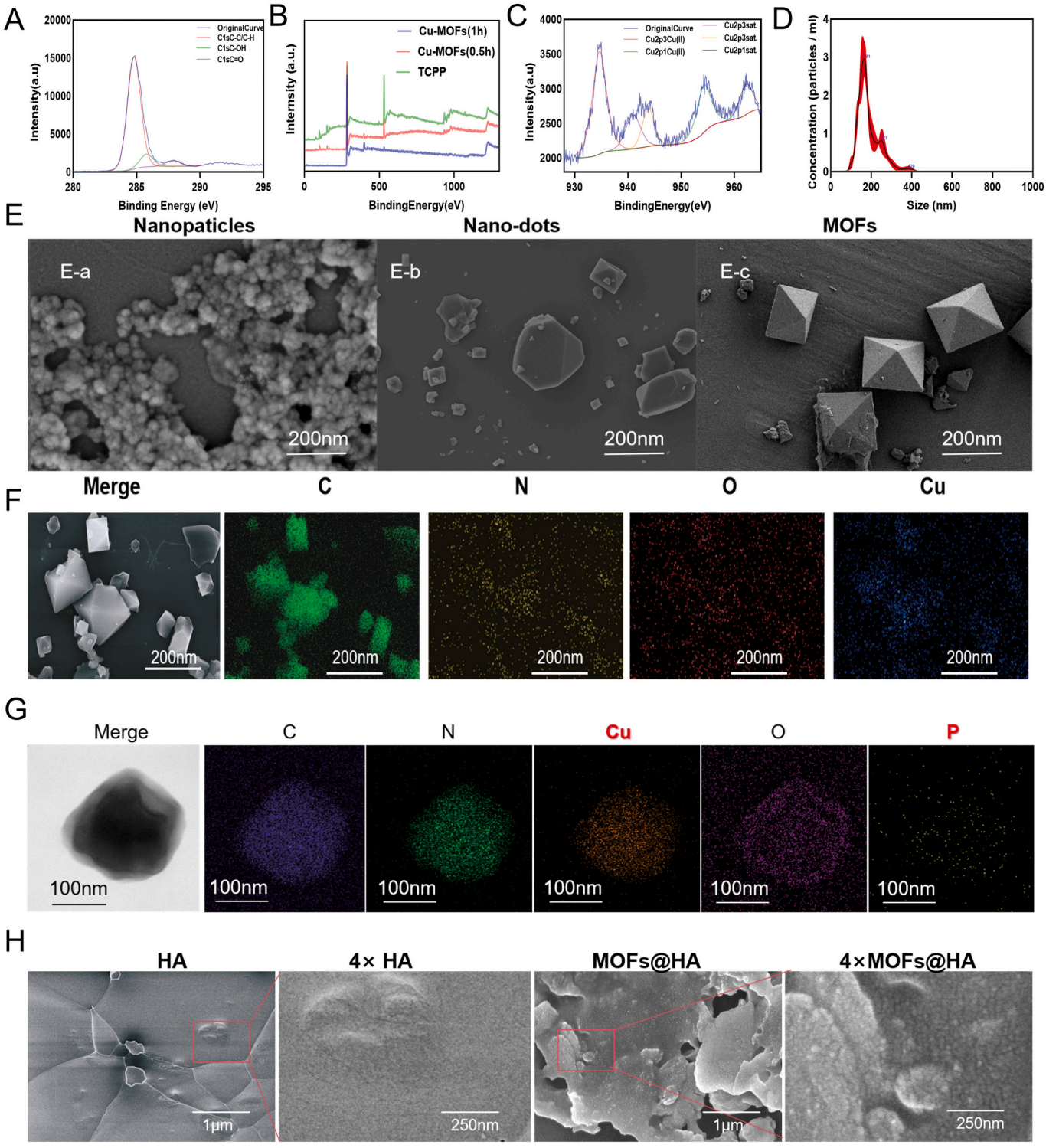

Fig. 1. (A) X-ray photoelectron spectroscopy in the Cu-MOFs structure. (B) The high-resolution Cu 2p spectrum Cu-MOFs. (C) The O^{1s} spectrum Cu-MOFs structure. (D) particle size of Cu-MOFs. (E) SEM of Cu-MOFs. (F) Elemental mapping of a single Cu-MOFs crystal, showing the homogeneous distribution of Cu (red), C (green), O (blue), and N (yellow). (G) TEM and mapping of Cu-MOFs within ANPs,Cu (orange), C (purple), O (red), N (green) and P (yellow). (H) SEM surface scan of Cu-MOFs encapsulated in hyaluronic acid hydrogel.

systematic investigation of the platform's spatiotemporal drug release kinetics, immune reprogramming mechanisms, and therapeutic synergies in CRC models, this work establishes a blueprint for engineering nature-derived hybrid nanomaterials. Our findings not only advance CRC combination therapy but also provide fundamental insights into the rational integration of biological and synthetic components for next-generation cancer nanomedicine (Scheme 1).

2. Results and Discussion

2.1. Physicochemical properties of Cu-MOFs

By X-ray photoelectron spectroscopy (Fig. 1A), the O^{1s} characteristic peaks of C═O and C-OH groups in pure tetracarboxyphenylporphyrin (TCPP) were located at 287.0 eV and 285.0 eV, respectively, while the uniform distribution of Cu elements in the and Cu-MOFs (Fig. 1A) confirms the successful coordination of the Cu ions with TCPP ligands. The high-resolution Cu 2p spectrum (Fig. 1B) showed Cu $2p_{3/2}$ binding energies of 935.2 eV and Cu $2p_{1/2}$ 955.1 eV and satellite peaks, which clarified the coordination state of Cu^{2+}.The O ^{1s} spectrum (Fig. 1C) showed that the C═O 531.6 eV and C-OH 533.3 eV The change in peak area indicates increased exposure of hydroxyl groups after ultrasonic stripping. The NTA (Nanoparticle Tracking Analysis) showed a primary peak with an average diameter of 190 nm indicating a moderate size distribution. The minor larger-size population likely corresponds to a small fraction of incompletely exfoliated aggregates, which is common in the processing of 2D nanomaterials. Scanning electron microscopy (SEM) images reveal that the synthesised Cu-MOFs form well-ordered octahedral micrometres crystals (Fig. 1E). As demonstrated in Supplementary Fig. S1, consistent crystal morphologies are observed across different fields of view, indicating excellent reproducibility of the synthesis method. The SEM elemental distribution map (Fig. 1F) further verified the homogeneous dispersion of Cu, C, O, and N.TEM morphology and mapping characterisation further revealed the encapsulation morphology of Cu-MOFs within ANPs, with simultaneous detection of P and Cu elements confirming successful encapsulation (Fig. 1G). Ultimately, the hyaluronic acid hydrogel-encapsulated Cu-MOFs (Fig. 1H) formed a reticulated composite structure, which, combined with its square-crystal morphology and homogeneous elemental distribution, elucidated the synthetic pathway from the self-assembly of organic ligands to the nano-framework, laying the foundation for the functionalized application. The copper loading capacity in the Cu-MOFs, as determined by ICP-OES, was found to be 3.95 wt% (Fig. S6).

2.2. Extraction and isolation of ANPs

Nanoparticle tracking analysis (NTA) showed that the particle size of ANPs was about 200 nm (Fig. 2A), and the zeta potentials of their vesicles with Cu-MOFs were distributed in the range of −5 to −18 mV (Fig. 2B)It is noteworthy that the size range of plant-derived nanoparticles is typically broader than that of animal exosomes, with values reported between 50 and 500 nm. The ANPs obtained in this study fall within this typical range [27]. Compositional analysis showed that the ANPs mainly contained ginsenoside Rb1 (Fig. 2C), which is the core active substance of American ginseng (Fig. 2D,E). A 45 % sucrose layer was isolated from fresh American ginseng by density gradient centrifugation as ANPs for experiments. Transmission electron microscopy (TEM) comparison of ANPs extracted from different sucrose gradients (45 %, 35 %, 25 %) revealed that the particles in the 45 % layer were morphologically intact and had the least impurities (Fig. 2F). Further, the ANPs were encapsulated into HA hydrogels, and it was seen that the ANPs were uniformly dispersed within the reticular skeleton of HA (Fig. 2G). The above results confirmed that the ANPs extracted from 45 % sucrose layer possessed homogeneous particle size, suitable surface charge and high purity of active ingredients, which provided a physicochemical basis for their composite application with HA hydrogel [27]. Given the absence of recognised specific protein markers for plant vesicles, their identification relies primarily on a combination of physical characterisation and the identification of characteristic functional components.

2.3. Synthesis and property analysis of HA hydrogels

Chemical cross-linking was successfully constructed by cross-linking HA with 1-ethyl-3-(3-dimethylaminopropyl) carbodiimide (EDC)/N-hydroxysuccinimide (NHS) (HA carboxyl:EDC:NHS = 1:2:1, stirred for 2 h at room temperature) and introducing cystamine (HA carboxyl: cystamine amino = 1:1) into the HA hydrogel network (Fig. 3A). First, cystamine-modified hyaluronic acid was synthesised via the condensation reaction of hyaluronic acid, EDC, NHS, and cystamine. The reaction was completed at room temperature under magnetic stirring for 1.5 h. Following dialysis in ultrapure water for one day, purified cystamine-modified hyaluronic acid was obtained. Subsequently, an excess of EDC was added under magnetic stirring at room temperature for two hours. After freeze-drying, the product was stored in a vacuum environment for subsequent use. Atomic force microscopy (AFM) showed that the ANPs engulfed the MOFs to form a monodisperse spherical structure (Fig. 3B), with an average height of about 12 nm (Fig. 3C), and the Young's modulus reached 4000 mPa, which was significantly higher than that of the liposomes, indicating that the complexes possessed high mechanical stiffness (Fig. 3D). The resonance peaks at δ 2.63 ppm and δ 2.85 ppm in the ANPs+MOFs@HA spectrum are attributed to the methylene C—H bonds of cystamine (CSA), confirming the successful synthesis of HASH (Fig. 2E).Equilibrium water content (EWC) experiments showed that the water holding capacity of ANPs+MOFs@HA was as high as 80–100 % (Fig. 3F). In the active ingredient release study, ginsenosides Rb1 and Re in the ANPs+MOFs group reached steady state after 60 h of release (Fig. 3G), whereas Rb1 in the ANPs+MOFs@HA group reached steady state after 200 h, demonstrating significant slow-release properties (Fig. 3H). Fourier Transform Infrared Spectroscopy (FTIR) showed the presence of hydroxyl (~3300 cm^{-1}), amide (~1650 cm^{-1}) and carboxylic acid (~1600–1400 cm^{-1}) characteristic peaks in the complexes, confirming the successful introduction of HA; metal-oxygen bonding of MOFs (400–600 cm^{-1}) peaks and carboxylic acid peaks were shifted and hydroxyl peaks were broadened, further verifying the three chemical interactions. Stability tests showed that ANPs+MOFs@HA remained structurally stable within 12 h (Fig. 3I), and free cystamine could be cleared by dialysis within 70 min (Fig. 3J) and was efficiently released in both PBS and collagenase mimetic solution (Fig. 3K). Swelling experiments showed that the complexes swelled about 10-fold in volume (Fig. 3L), and the storage modulus (G′) was consistently higher than the loss modulus (G″) in rheological tests (0.1–100 Hz), confirming hydrogel network formation (Fig. 3M). Disulfide bond cross-linking enhanced structural stability (Fig. 3N), and release curve fitting (Fig. 3P,Q) demonstrated that Rb1 and Re followed a nonlinear kinetic release mechanism, consistent with diffusion-solubilisation synergy in complex drug-carrying systems. Scanning electron microscopy revealed that pure HA hydrogel formed a relatively dense film upon drying, whereas ANPs+MOFs@HA exhibited a characteristic porous network structure (Fig. 2G and Fig. 3). This porous architecture arises from the incorporation of ANPs and MOFs, which act as heterogeneous nucleation sites during chemical cross-linking and subsequent drying. This promotes phase separation within the polymer network, yielding a three-dimensional porous framework conducive to mass exchange. We further investigated the drug release kinetics of the ANPs+MOFs@HA composite. As depicted in Fig. 3F and G, the HA hydrogel markedly retarded the release of the active components ginsenosides Rb1 and Re from the ANPs. Furthermore, we characterised the behaviour of the MOFs by monitoring Cu^{2+} release. The results (Fig. S5) revealed a slow release of Cu^{2+} from the composite hydrogel, exhibiting sustained-release characteristics over 28 h(Fig. S8), indicating that this platform enables controlled delivery of therapeutic components.

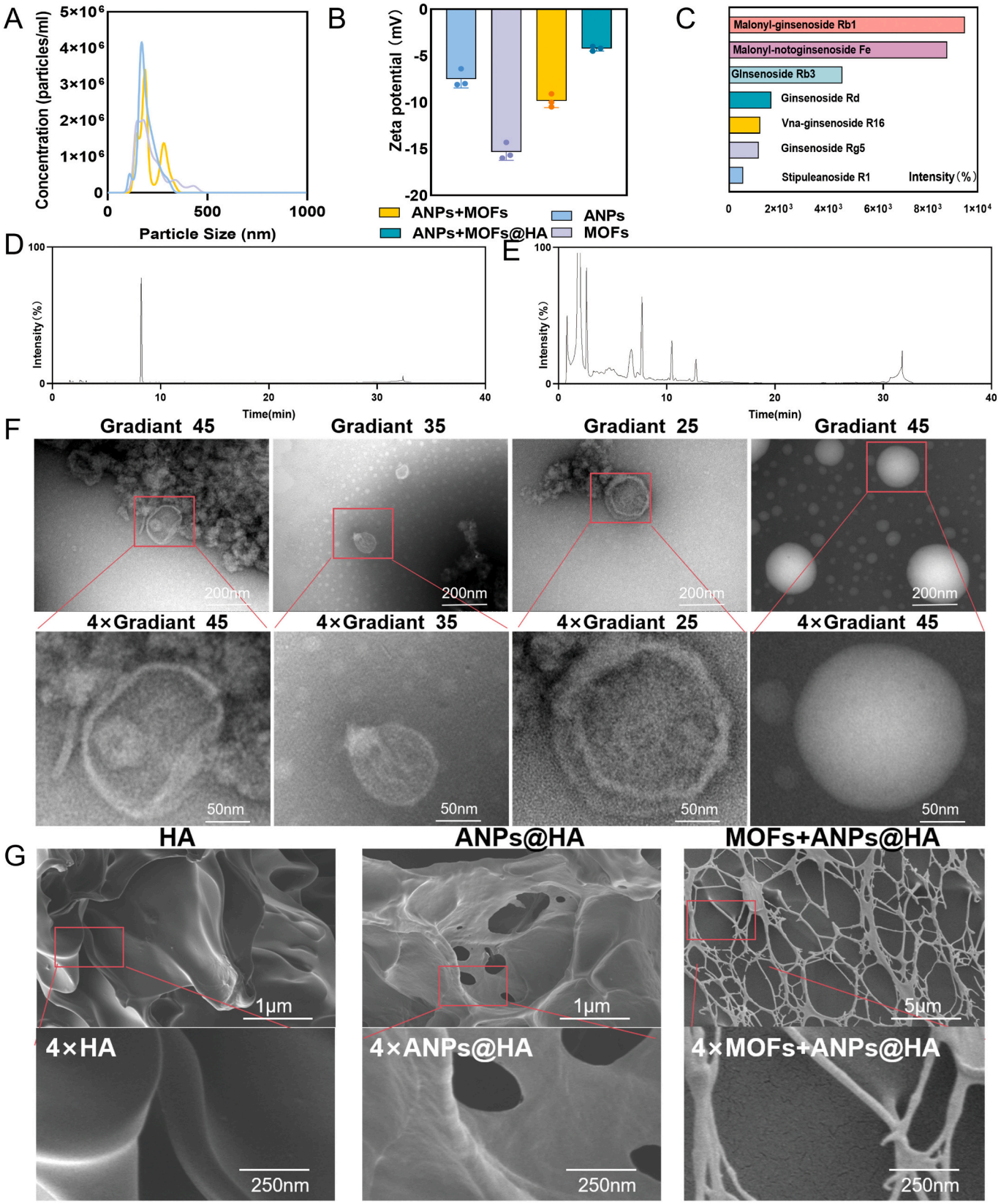

Fig. 2. Extraction and characterisation of ANPs. (A) NTA particle size of ANPs, (B) zeta potentials of ANPs and MOFs, MOFs phagocytosed by ANPs and ANPs+MOFs@HA, (C) Seven compounds with the highest distribution in the 45 % sucrose fractionation layer, (D) Liquid chromatograms of ginsenoside Rb1. (E) liquid chromatogram of ANPs, (F) TEM electron microscope images of ANPs in 45 %, 35 %, and 25 % sucrose solution and TEM electron micrographs of ANPs in the 45 % layer without negative staining, (G) SEM cross-sections of the loading morphology of ANPs before and after phagocytosis of MOFs in hydrogels.

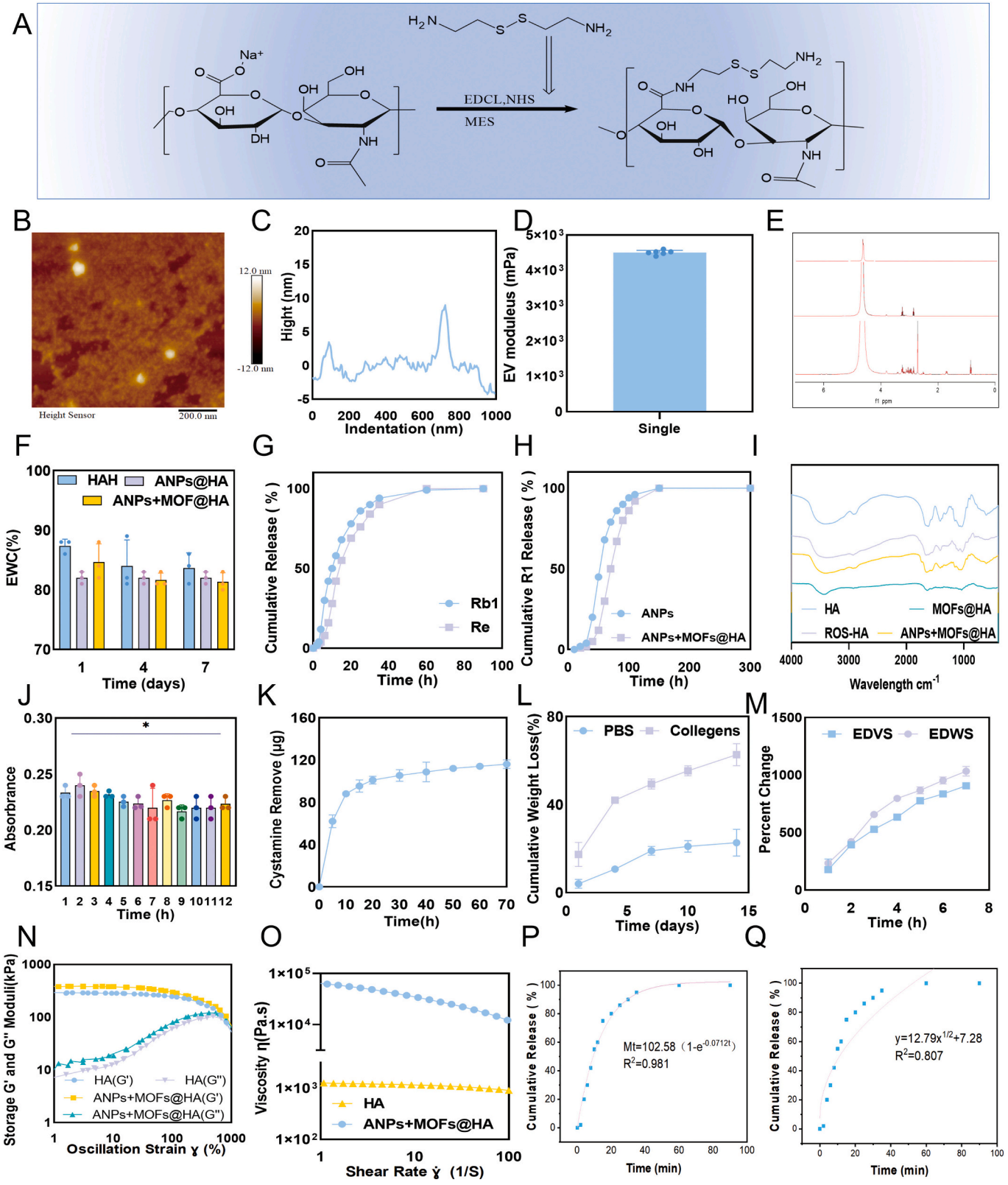

Fig. 3. Synthesis and properties of ANPs+MOFs@HA. (A) Synthesis route of ANPs+MOFs@HA, (B) Atomic particle morphology of ANPs+MOFs, (C) Particle height of ANPs+MOFs, (D) Single-particle modulus of ANPs+MOFs, (E) NMR spectra before and after the synthesis of ANPs+MOFs@HA. (F) Water retention before and after the encapsulation of ANPs+MOFs@HA, (G) Release of ginsenosides Rb1 and Re from ANPs+MOFs, (H) Release of ginsenoside Rb1 from ANPs+MOFs@HA, (I) FTIR spectra of ANPs+MOFs@HA before and after encapsulation, (J) UV absorption of ANPs+MOFs@HA over 12 h, (K) Free cystamine scavenging in ANPs+MOFs@HA, (L) Water loss of ANPs+MOFs@HA in PBS and Collegens, (M) Water loss in ANPs+MOFs@HA and HA, (L) Dissolution index of ANPs+MOFs@HA and HA, (N) Young's modulus before and after cross-linking of ANPs+MOFs@HA, (O) Rheology of ANPs+MOFs@HA before and after cross-linking of ANPs+MOFs@HA, (P) Release curve fitting of ginsenoside Rb1, (Q) Release curve fitting of ginsenoside Re. Data are presented as means ± SD ($n = 3$). *$P < 0.05$.

2.4. Targeted delivery and biosafety of ANPs+MOFs@HA

The results showed that ANPs+MOFs@HA exhibited multi-pathway synergistic effects in colon cancer treatment. After 12 h of starvation in mice, DiR-labelled ANPs+MOFs@HA was administered to the colon (Fig. 4A), and immunofluorescence showed that it could be efficiently taken up by CT26 colon cancer cells and RAW264.7 macrophages. FITC-labelled ANPs+MOFs@HA significantly inhibited the expression of intracellular reactive oxygen species (ROS) (Fig. 4B), which demonstrates the intrinsic antioxidant properties of ANPs+MOFs@HA under non-irradiated conditions, as evidenced by significant inhibition of intracellular ROS levels. This suggests a potential protective role against oxidative stress in the absence of photodynamic activation. ANPs+MOFs@HA-labelled ANPs can be targeted to CT26 cells and RAW264.7 cells, as shown in Fig. 4C.This provides strong evidence for further elucidating the mechanism of action of ANPs+MOFs@HA. MTT assay showed that the low dose (1 μg/mL)ANPs+MOFs@HA can promote RAW264.7 proliferation and inhibition CT26 growth (Fig. 4D,E,F) and remained biosafe at 150 μg/mL (Fig. 4G). Further analysis of inflammatory factors revealed that ANPs+MOFs@HA significantly upregulated the RNA expression of anti-inflammatory molecules TNF-α, IL-12, IL-1β, IL-6 and IFN-γ (Fig. 4J-N), suggesting that it inhibited inflammatory responses by regulating the immune micro-environment. In summary, ANPs+MOFs@HA synergistically inhibited colon cancer progression through a dual mechanism of direct killing of CT26 cells and activation of macrophages, while combining low toxicity and targeted delivery properties, providing a novel strategy for colon cancer treatment. Importantly, upon 650 nm laser irradiation (100 mW/cm^2, 5 min), ANPs+MOFs@HA induced a dramatic increase in intracellular ROS levels in CT26 cells compared to non-irradiated controls (Supplementary Fig. S4), confirming its potent photodynamic activity. To validate the photodynamic capability of ANPs+MOFs@HA, we measured intracellular ROS levels in CT26 cells using DCFH-DA flow cytometry. Upon 650 nm laser irradiation (5 min), ANPs+MOFs@HA induced a dramatic 4-fold increase in ROS levels compared to the control group ($p < 0.01$), and significantly outperformed free MOFs + laser ($p < 0.01$) (Fig. 4H,I). Crucially, without laser exposure, ANPs+MOFs@HA showed minimal ROS induction, confirming its light-triggered ROS generation mechanism [28].To validate the intrinsic antioxidant properties of ANPs+MOFs@HA under non-illuminated conditions, we assessed its radical scavenging capacity. As shown in Supplementary Fig. S7, ANPs themselves exhibited potent DPPH and ABTS radical scavenging activity, consistent with results from the known antioxidant ginsenosides they contain (Fig. 2C-E). Notably, the ANPs+MOFs@HA composite also retained significant antioxidant capacity, whereas Cu-MOFs alone exhibited no such functionality. This unequivocally demonstrates that the platform's antioxidant properties derive from the natural bioactive constituents within the ANPs, thereby aiding in the alleviation of baseline oxidative stress within the tumor microenvironment during non-treatment periods. The intrinsic antioxidant property of the ANPs+MOFs@HA platform under non-irradiated conditions is attributed to the radical-scavenging bioactive molecules encapsulated within the ANPs.

2.5. Therapeutic effect of ANPs+MOFs@HA in in vivo CRC model

CT26 cells were injected to construct a mouse model of colon cancer, and in this study, the mice were randomly divided into six groups: the Control group, the Model group, the ANPs group, the MOFs group, the ANPs+MOFs@HA group and the HA group. All groups were administered by gavage, and the ANPs+MOFs@HA group was combined with 650 nm laser irradiation (100 mW/cm^2, 20 min/day). After 8 days of intervention (Fig. 5A), mice in the ANPs+MOFs@HA group showed a significant slowdown in tumor volume growth (Fig. 7B), an improved trend in body weight loss (Fig. 5C), a reduction in colonic histopathological damage (Fig. 5D), a decrease in the disease activity index (DAI) (Fig. 5E), and lower spleen weight and myeloperoxidase (MPO) levels than those of the model group (Fig. 5F,G), suggesting that it effectively alleviating colonic inflammation and tumor progression. Colonic inflammatory factor assays (Fig. 5H) showed that ANPs+MOFs@HA significantly inhibited the expression of pro-inflammatory factors IL-1β, TNF-α and iNOS, while up-regulating the immunosuppressive factor IL-10 and the pro-inflammatory factor IL-12.The concurrent increase in IL-10 (Fig. 5I), often associated with M2 macrophages, may reflect a regulatory feedback mechanism or the presence of a subpopulation of regulatory macrophages within the shifted microenvironment, contributing to resolution of inflammation while maintaining anti-tumor activity. Within 14 h, ginsenoside Rb1 (Fig. 5I) and ginsenoside Re (Fig. 5J) exhibited differing retention levels in mouse tissues, with delivery to tumor sites achievable within 3 h. Pharmacokinetic analyses (Fig. 5K,L) demonstrated that ANPs+MOFs@HA increased the accumulation of ginsenosides Rb1 and Re in tissues, and delayed their metabolic clearance rate. In conclusion, ANPs+MOFs@HA demonstrated a multi-pathway anti-colon cancer potential by inhibiting tumor proliferation, modulating the inflammatory micro-environment and prolonging the duration of drug action.

2.6. Molecular mechanisms of pharmacological inhibition of enteritis

ANPs+MOFs@HA were efficiently delivered to the intestinal epithelial target region (Fig. 6A), which is enriched with macrophages and may be related to its immunomodulatory function. We evaluated the efficacy of different treatment groups in inducing tumor cell apoptosis by detecting the protein levels of Caspase-3. As shown in Fig. 6B, there were significant differences in the ability to induce apoptosis among the treatment groups. This suggests that Cu-MOFs may be the most effective component for inducing tumor cell apoptosis, but its therapeutic effect cannot be fully realized in a simple physical mixture system. Only by co-encapsulating it with ANPs within HA hydrogels to form the ANPs+MOFs@HA composite material can effective synergistic interactions and spatiotemporal controlled release between components be achieved. This restores and optimizes its potent apoptosis-inducing capacity, ultimately delivering optimal tumor therapeutic outcomes. Histopathological analysis showed that the control group had regular cellular arrangement and homogeneous collagen distribution, while the inflammatory infiltration and collagen deposition were significantly reduced in the ANPs+MOFs@HA treatment group (Fig. 6C), suggesting that the combination system alleviated the pathological damage through synergistic effects and the HA modification further optimised the therapeutic efficacy. In addition, AB-PAS staining showed that ANPs+MOFs@HA inhibited intestinal fibrosis and mucus secretion abnormality (Fig. 6D), suggesting that it slowed down the disease process by targeting and regulating epithelial-mesenchymal interactions. Histopathological analysis revealed that ANPs+MOFs@HA treatment significantly alleviated colitis-induced inflammatory damage and fibrosis, objectively confirmed by a marked reduction in semi-quantitative histological scores. The above results collectively indicated that ANPs+MOFs@HA improved the pathological features of colon cancer in a multidimensional manner by enhancing targeted delivery, modulating the immune micro-environment and inhibiting fibrosis.

2.7. Drug distribution and accumulation

Observations at 0 h, 2 h, 6 h, 12 h, 24 h showed that the effect of ANPs+MOFs@HA was gradually enhanced with time (Fig. 7A). Tumor volume change curves showed that the ANPs+MOFs@HA group showed significantly better tumor suppression effect than other treatment groups within 20 days (Fig. 7B, C).ANPs+MOFs@HA showed no significant accumulation toxicity in heart, liver, spleen, lung and kidney, Fig. 7E. Further comparison of the performance of ANPs, ANPs@HA, ANPs+MOFs@HA in Fig. 7D,F, confirmed that ANPs+MOFs@HA had

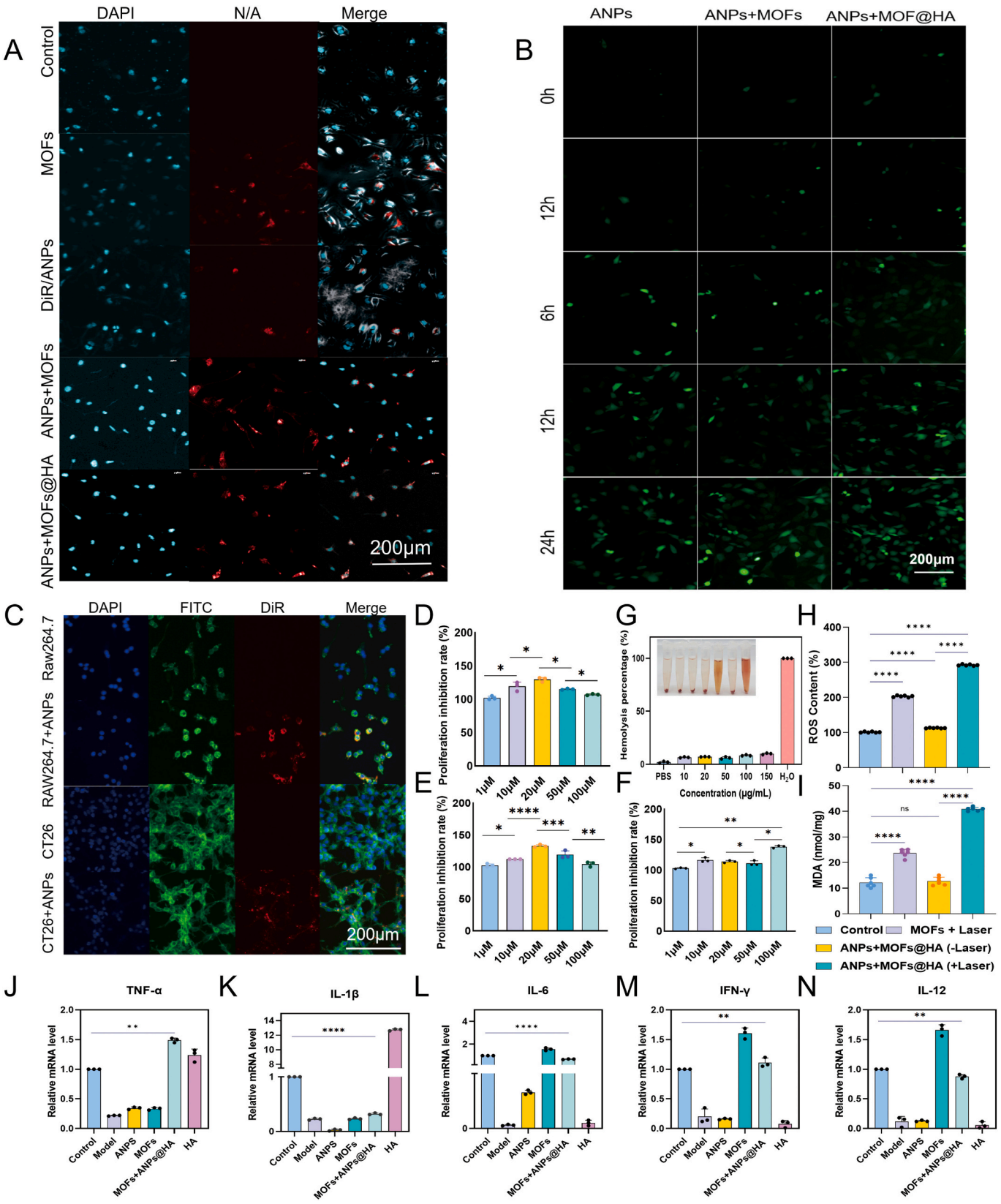

Fig. 4. Targeting ability study of ANPs+MOFs@HA (A) Targeting of ANPs+MOFs@HA to CT26 cells, (B) ROS changes before and after ANPs+MOFs@HA encapsulation, (C) Uptake of ANPs by RAW264.7, RAW264.7 + ANPs, CT-26, and CT-26 + ANPs (Scale bar = 50 μm) (D) MTT cell proliferation assay was used to assess the effect of ginsenoside Rb1, (E) Ginsenoside Re and (F) ANPs+MOFs@HA on RAW264.7 cell proliferation. (G) Cytotoxicity expression levels of ANPs+MOFs@HA,(H)Light-triggered ROS generation in CT26 cells. Cytotoxicity expression levels of ANPs+MOFs@HA, Cytokine of RAW264.7 on TNF-α (J), IL-1β (K), IL-6 (L),IFN-γ (M), IL-12 (N). (I) Flow cytometry analysis of DCF fluorescence intensity.

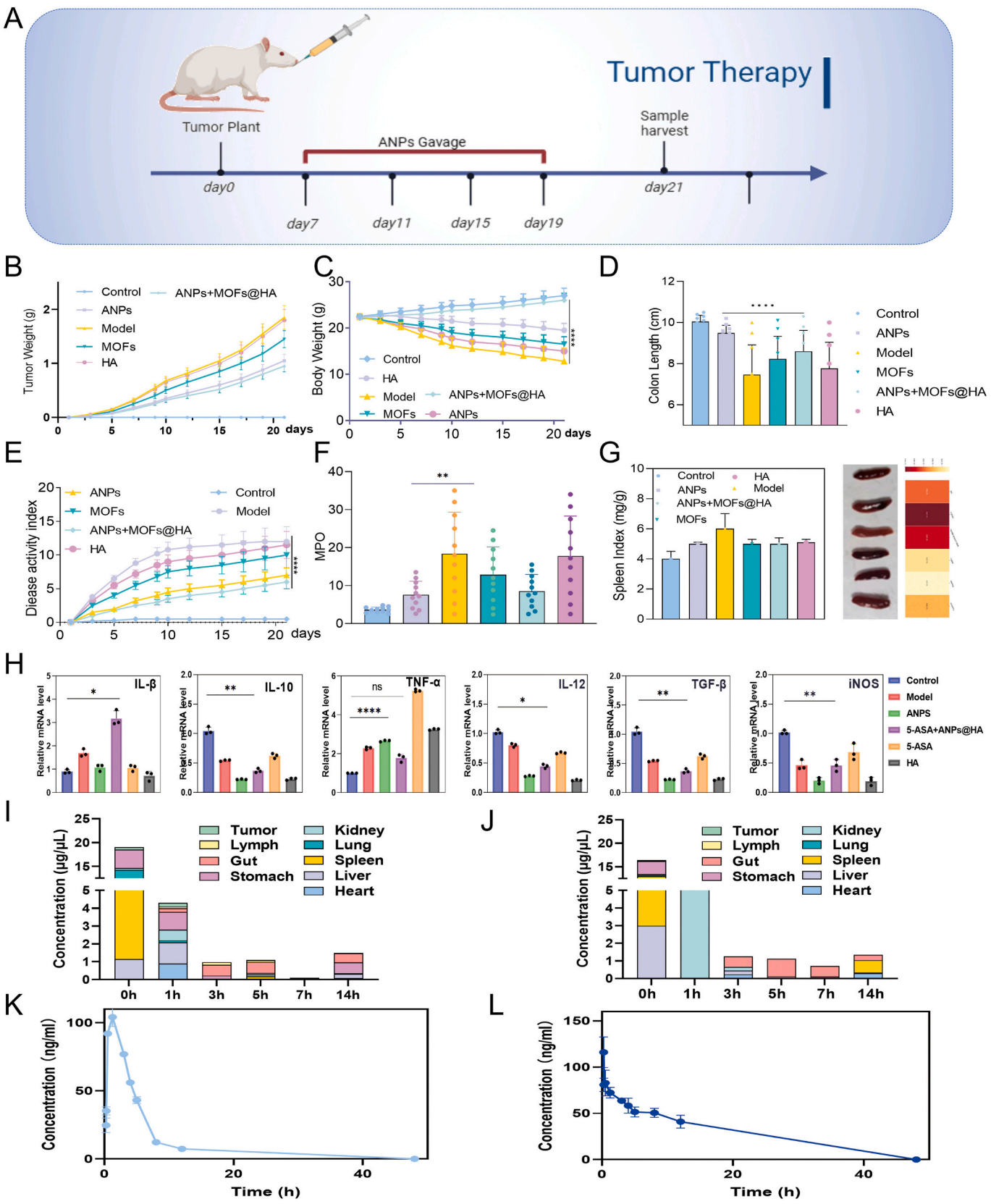

Fig. 5. Efficacy of ANPs+MOFs@HA in a mouse model of colon cancer. (A) Animal experimental protocol. (B) Detailed recordings of daily tumor volume. (C) Body weight changes. (D) Colon length, (E) DAI scores, and (F) MPO activity and analysed, $n = 6$. (G) Spleen indices for each group.(H) Measurements and analyses of splenic weights, n = 6. inflammatory factor IL-1β,IL-10,TNF-α,IL-12,TFG-β,iNOS expression levels.(I) Tissue distribution of ginsenosides Rb1.(J) and Re(M) over 14 h. (K) Pharmacokinetic profiles of ginsenosides Rb1 and ANPs+MOFs@HA administered orally. (L) Pharmacokinetic profiles of ginsenosides Rb1 and ANPs+MOFs@HA administered intravenously.

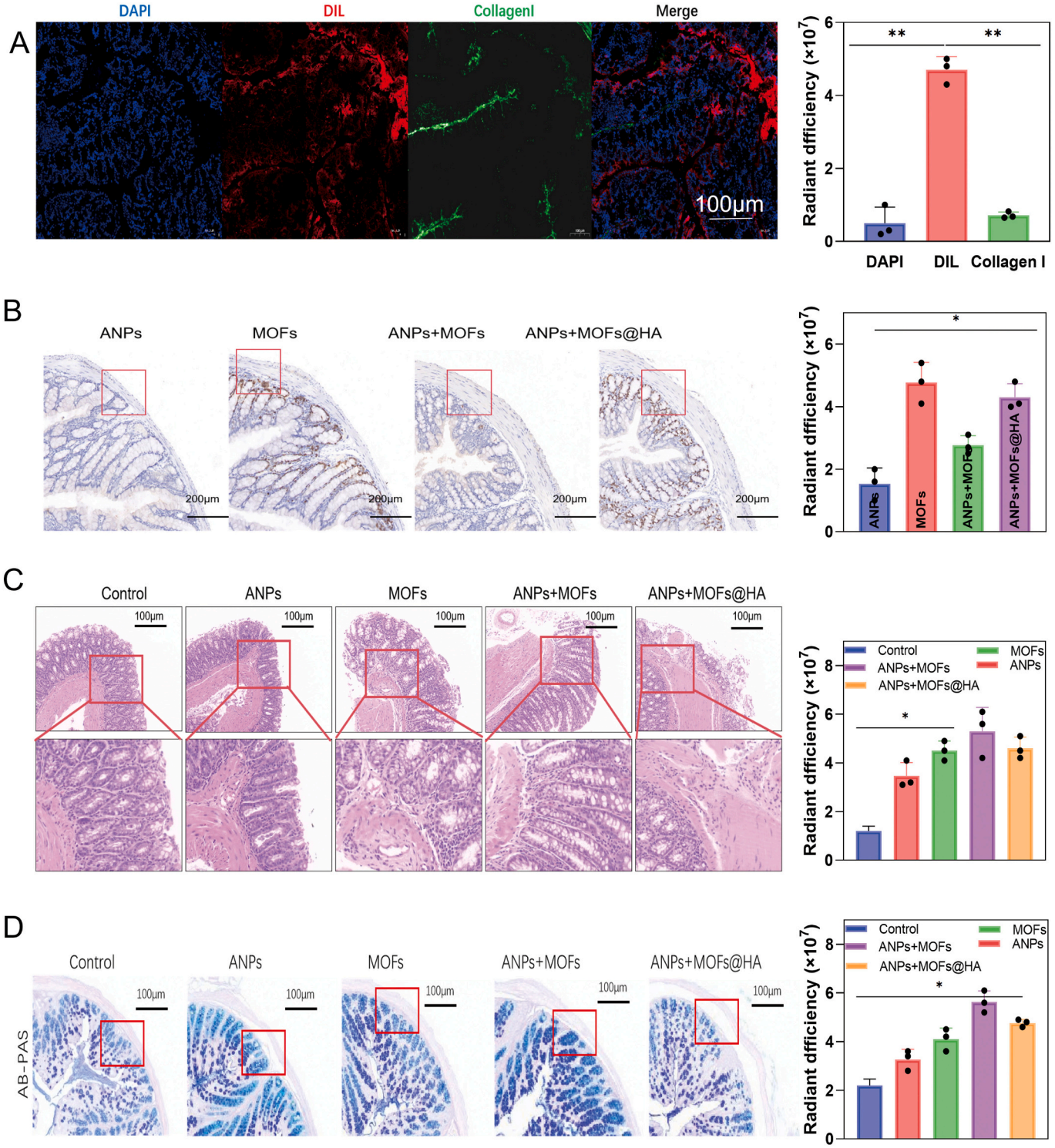

Fig. 6. ANPs+MOFs@HA inhibit intestinal inflammation. (A) Distribution area of ANPs in colonic tissues, (B) immunohistochemical map of Casepase3 in colonic tissues. (C) Comparison of therapeutic effects before and after ANPs+MOFs@HA encapsulation, (D) AB-PAS maps in colon tissues before and after ANPs+MOFs@HA encapsulation.

superior stability and targeting properties. The fluorescence co-localisation images showed that ANPs+MOFs@HA was uniformly distributed within the cell with no significant overlap with the nucleus, suggesting that it may function through the cytoplasmic pathway. Thus, ANPs+MOFs@HA exhibited efficient antitumour activity, low organ toxicity and good intracellular delivery properties.

2.8. Mechanism of colon cancer inhibition by ANPs+MOFs@HA

Analysis of the spatiotemporal distribution of the active ingredient after oral administration demonstrated that ANPs+MOFs@HA achieved targeted accumulation in the tumor region of colon cancer model mice between 1 h and 2 h range (Fig. 8A). Metabolomic analysis revealed significant differences in the metabolite profiles between the tumor

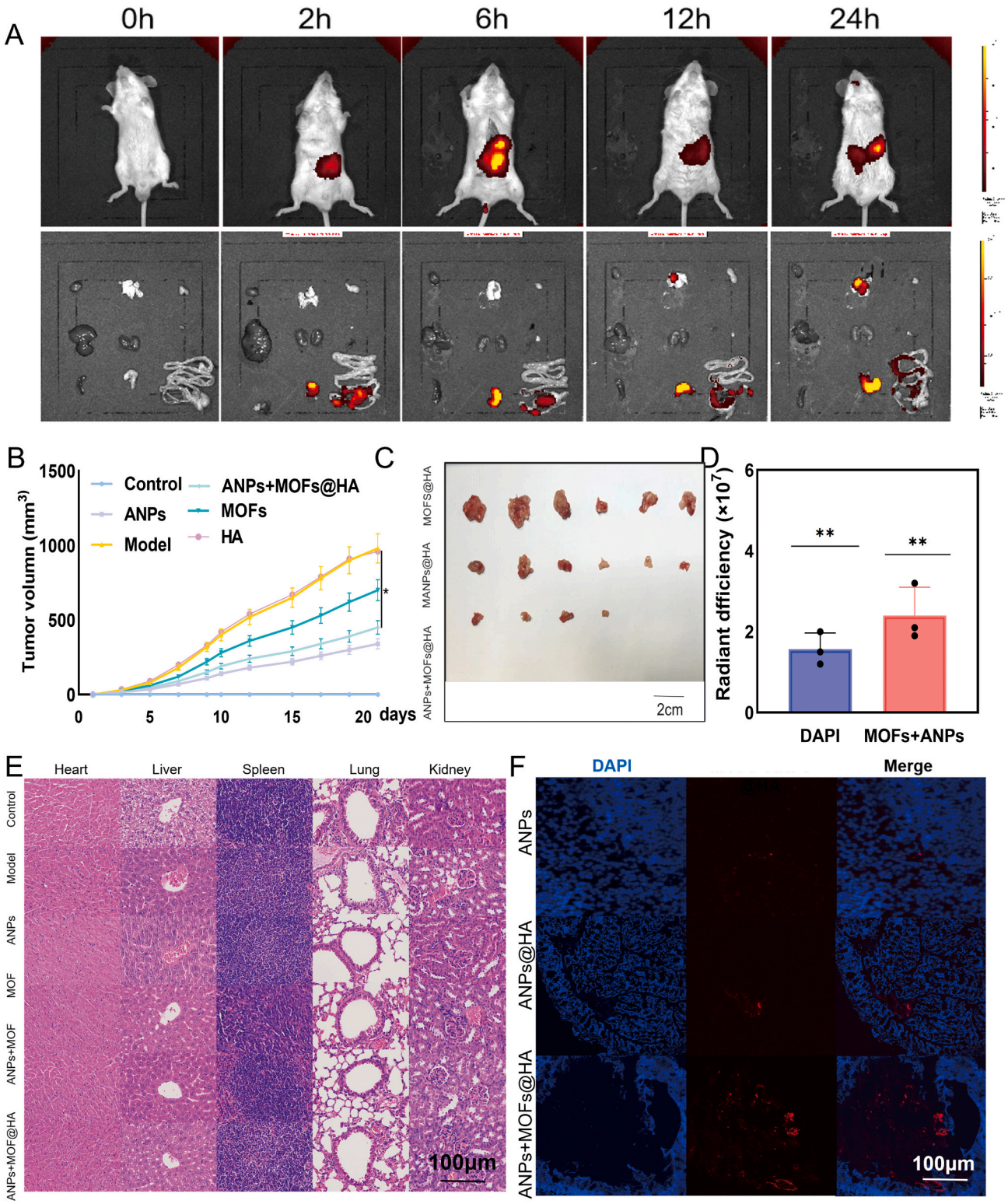

Fig. 7. Spatial distribution and accumulation of ANPs+MOFs@HA. (A) Distribution area of ANPs+MOFs@HA in colonic tissues, (B) colonic volumes and photographs of loaded mice (C)Tumor volume of mice.(D)Statistical graph of fluorescence intensity in colon immunofluorescence.(E) pathological maps of heart, liver, spleen, lungs, and kidneys after ANPs+MOFs@HA intervention.(F) Accumulation in intestinal tissues before and after ANPs+MOFs@HA encapsulation in the colon.

region and the model group 2 hours post-administration (Fig. 8B), validated by distinct metabolite clustering patterns between tumor cell and fibroblast regions (Fig. 8C). Principal component analysis (PCA) and OPLS-DA maps revealed distinct metabolite distributions (Fig. 8D,E). Notably, both the pantothenic acid-CoA biosynthesis pathway (Fig. 8F) and L-carnitine activity (Fig. 8K) were downregulated, suggesting metabolic reprogramming may drive macrophage polarization toward the M1 phenotype (Fig. 8I). The downregulation of the pantothenic acid-CoA biosynthesis pathway and *L*-acetylcarnitine indicates disrupted fatty acid oxidation (FAO) and acetyl-CoA metabolism within the tumor

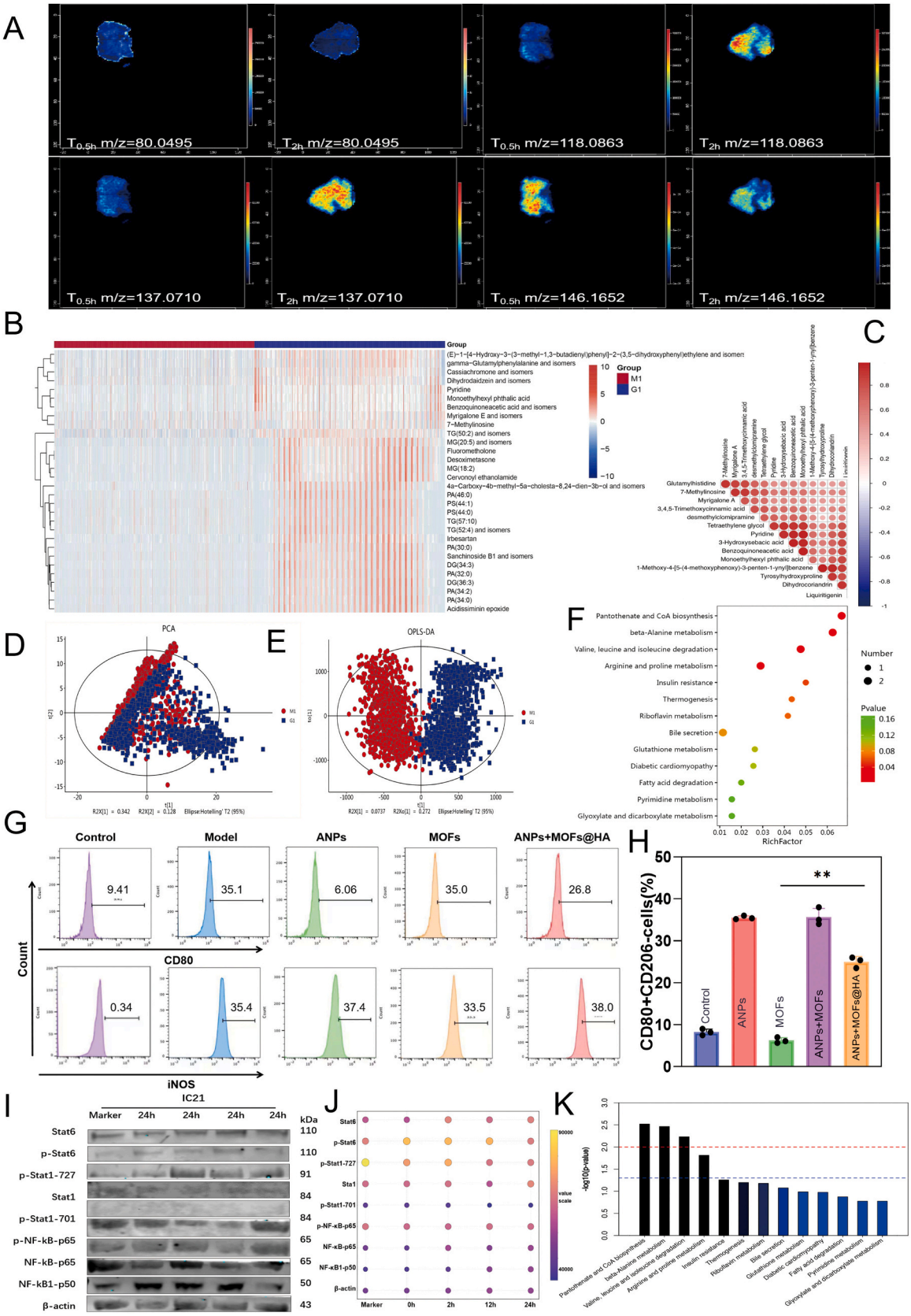

Fig. 8. Anti-tumor mechanism of ANPs+MOFs@HA. (A) Distribution regions of ANPs active components in tumor tissues, (B) Metabolite enrichment maps in the model and ANPs+MOFs@HA intervention groups, (C) Functional enrichment maps in the model and ANPs+MOFs@HA intervention groups, (D),*PCA* and (E) *OPLS-DA* of metabolites in the model and ANPs+MOFs. (F) Model group and ANPs+MOFs@HA intervention group functional enrichment statistics. (G) Flow plots and (H) column plots of iNOS before and after ANPs+MOFs@HA intervention, (I) ANPs+MOFs@HA post-intervention western-blot. (J) Western-blot statistical bubble chart. (K) Functional enrichment column in the model and ANPs+MOFs@HA intervention groups,

microenvironment. Previous studies have established a link between metabolic reprogramming and macrophage function: impaired fatty acid oxidation and acetyl-CoA supply can drive macrophages from the M2 phenotype to a substitute activation state. These metabolic alterations likely contributed to the observed reprogramming of macrophages toward an M1 phenotype (Fig. 8G,H), where MOFs significantly reduced iNOS expression and remodeled the immunosuppressive tumor microenvironment. Western blot analysis further confirmed that ANPs+MOFs@HA remodeled the tumor immune microenvironment by inhibiting the NF-κB signaling pathway (Fig. 8I,J) and reducing proinflammatory factor release. These findings demonstrate that ANPs+MOFs@HA enhance antitumor activity through synergistic effects of spatiotemporal-specific delivery, metabolic regulation, and macrophage polarization.

3. Experimental section

3.1. Synthesis of Cu-MOFs

Preparation of mixed solution: a certain amount of TCPP and copper salt were weighed in a beaker, appropriate amount of DMF was added as solvent and mixed well. The pH of the solution was adjusted to 5.5 to promote the formation of specific MOFs structures. Solvothermal reaction was carried out at 80 °C for 5 h [27]. The solid products of MOFs were collected using vacuum filtration. The solid product was washed several times using DMF, and the washed MOFs were dried at room temperature or at a slightly elevated temperature to remove residual solvent. The synthesised MOFs were characterised using techniques such as XPS, SEM, TEM, and specific surface area analysis to confirm their structure and morphology [29].

3.2. Extraction and characterisation of ANPs

Fresh American ginseng roots. Sterile PBS or other suitable extraction buffer. The ginseng was cleaned to remove soil and impurities. Cut the American ginseng into small slices and remove large impurities by centrifugation at1000g. The supernatant is transferred to a new centrifuge tube and 100,000 *g* ultra-centrifuged to collect plant vesicles. After centrifugation, the vesicles are deposited at the bottom of the tube and the precipitate is collected. The precipitate is washed with sterile PBS to remove residual cellular debris and proteins. Ultra-centrifugation was performed again, then the supernatant was removed and the vesicle precipitate was retained. The collected ANPs were resuspended in an appropriate amount of sterile PBS for subsequent experiments. The resuspension was filtered through a 0.22 μm filter membrane to ensure vesicle homogeneity and remove bacterial contamination [30]. TEM: to observe the morphology and size of ANPs.AFM: to assess the surface morphology and size of ANPs [31]. Particle size analysis [32]: dynamic light scattering (NTA): to determine the particle size distribution of ANPs. Determination of total protein content in ANPs using methods such as BCA protein quantification kit. Chemical composition analysis: Analyse the chemical composition in ANPs by liquid mass spectrometry (MS). Functional analysis: to assess the uptake capacity of ANPs in CT26 cells and their role in intercellular communication. Thermal and pH stability tests: to assess the stability of ANPs by incubation experiments at different temperature and pH conditions. Flow cytometry analysis: surface labelling of ANPs was analysed using flow cytometry 3.3 Preparation of hyaluronic acid hydrogels (HA).

3.3. Construction of ANPs+MOFs@HA composites

The condensation reaction was carried out by cystamine-modified HA by using condensation reaction solution (0.1 mmol/mL, pH 5.5) as solvent. The reaction was magnetically stirred for 3 h at room temperature and protected with nitrogen. Cystamine-modified HA was purified by dialysis in deionised water for 3 days. Subsequently, add excess tris (2-carboxyethyl)phosphine hydrochloride under magnetic stirring at room temperature for 3 h and protected with nitrogen. Cystamine-modified HA was purified by dialysis using hydrochloric acid solution for 3 days The dialysed solution was lyophilised and stored under vacuum until further use.

3.4. Drug release kinetic study

ANPs+MOFs@HA composite release medium. The composite containing drug ANPs+MOFs@HA was placed in a dialysis bag and sealed [33]. The dialysis bag was placed in a container containing the release medium at a constant temperature of 37 °C. Samples were taken periodically and replenished with fresh media. The concentration of the drug in the release medium was determined using high performance liquid chromatography HPLC and ultraviolet-visible spectroscopy UV–Vis [34]. Sampling time points were set according to the half-life and therapeutic window of the drug.

3.5. In vitro cell experiments

CT26 cells were cultured to 80–90 % density. The ANPs+MOFs@HA composites were macerated with PBS and co-cultured with cells to assess cellular uptake and toxicity. Cellular uptake was observed using fluorescently labelled composites and confocal microscopy. Cell viability was assessed using MTT assays. Set the dose according to the safety range for cellular experiments and previous studies.

3.6. In vivo CRC modelling and assessment of treatment efficacy

Balb/C mouse were randomly assigned to six groups (Control, Model, ANPs, MOFs, ANPs+MOFs@HA, HA), with six animals per group ($n = 6$). This sample size was determined based on our preliminary pre-experimental data. Colon cancer model was established using subcutaneous injection of 10^6 CT26 cells. Treatment experiment: animals were randomly divided into control and treatment groups by local administration of ANPs+MOFs@HA composites. Efficacy assessment: the animals were regularly observed for body weight and disease activity index (DAI) [35]. At the end of treatment, tissue samples were collected for pathological analysis. The therapeutic dose was set according to the results of the pre-tests and the pharmacokinetic properties of the drugs.

4. Conclusion

In this study, we successfully developed a composite material ANPs+MOFs@HA based on MOFs reinforced by ANPs and HA, and applied it to the treatment of CRC [36,37]. Through a series of material synthesis, characterisation and biological evaluation methods, we have thoroughly explored the potential and mechanism of ANPs+MOFs@HA in the treatment of CRC. We employed advanced material synthesis techniques, including solvothermal and ultracentrifugation, to prepare and purify MOFs and ANPs [38].By physical adsorption and chemical cross-linking, MOFs and ANPs were integrated into HA hydrogel networks to form composites with good biocompatibility. This study provides a strategic solution to the persistent challenges in CRC treatment, notably the poor efficacy of conventional therapies due to inadequate drug targeting, dose-limiting side effects, and an immunosuppressive TME [39]. Our approach of combining natural vesicles with synthetic materials offers a promising avenue to enhance therapeutic efficacy while minimizing systemic toxicity. The treatment of CRC, a chronic inflammatory bowel disease, requires new approaches to improve efficacy and patient quality of life [36]. We found that ANPs+MOFs@HA composites were effective in improving drug delivery efficiency and showed good biocompatibility and anti-inflammatory activity in in vitro cellular assays. In an in vivo CRC model, ANPs+MOFs@HA significantly reduced colonic inflammation, ameliorated colonic histopathological

damage, and promoted colonic mucosal repair. These results suggest that ANPs+MOFs@HA composites, as a novel drug carrier, can improve the efficacy of CRC treatment by enhancing drug targeting and reducing side effects. In addition, the preparation method and therapeutic mechanism of this material provide new perspectives for the treatment of CRC. This work not only provides a potential novel therapy for the treatment of CRC, but also provides a scientific basis for the use of natural plant-derived extracellular vesicles and metal-organic skeleton materials in biomedical applications. Future studies will focus on optimising the preparation process of ANPs+MOFs@HA composites, further exploring their dose-effect relationship in UC treatment, and conducting clinical trials to validate their safety and efficacy. In addition, we will also explore the potential application of this composite in the treatment of other inflammatory diseases. In conclusion, this study provides an innovative approach to CRC treatment, which opens up new avenues for enhancing therapeutic efficacy and improving patients' quality of life through the use of natural materials and advanced nanotechnology.

CRediT authorship contribution statement

Ling Weng: Writing – original draft. **Miao Wang:** Funding acquisition. **Yumeng Zhang:** Funding acquisition, Conceptualization. **Ruixiang Xu:** Visualization, Methodology, Investigation. **Min Zhao:** Funding acquisition. **Chunjie Zhao:** Writing – review & editing, Funding acquisition. **Yihe Huang:** Visualization.

Declaration of competing interest

The authors declare that they have no known competing financial interests or personal relationships that could have appeared to influence the work reported in this paper.

Acknowledgements

The research received financial backing from 1. Liaoning Provincial Department of Science and Technology Applied Basic Research Program Grant numbers: 2023JH2/101600013; 2. Liaoning Provincial Department of Education Basic Scientific Research Project Grant numbers: JYTMS20231376; 3. National Natural Science Foundation of China Grant numbers: 82505157; 4. Science and Technology Plan Project of Liaoning Provincial Department of Science and Technology Grant numbers: 2025-BS-0759.

Appendix A. Supplementary data

Supplementary data to this article can be found online at https://doi.org/10.1016/j.cej.2025.171664.

Data availability

Data will be made available on request.

References

[1] B. Thulasinathan, K.N. Suvilesh, S. Maram, E. Grossmann, Y. Ghouri, E.P. Teixeiro, J. Chan, J.T. Kaif, S. Rachagani, The impact of gut microbial short-chain fatty acids on colorectal cancer development and prevention, Gut Microbes 17 (2025) 2483780.
[2] B.W. Katona, A. Shukla, W. Hu, T. Nyul, C. Dudzik, A. Arvanitis, D. Clay, M. Dungan, M. Weber, V. Tu, F. Hao, S. Gan, L. Chau, A.M. Buchner, G.W. Falk, D. L. Jaffe, G. Ginsberg, S.N. Palmer, X. Zhan, A.D. Patterson, K. Bittinger, J. Ni, Microbiota and metabolite-based prediction tool for colonic polyposis with and without a known genetic driver, Gut Microbes 17 (2025) 2474141.
[3] M. Dai, X. Xiao, C.L.T. Guo, R.N. Lui, H.C. Yip, S. Chu, S.F. Hon, S.S.M. Ng, P.W. Y. Chiu, S.C. Ng, F.K.L. Chan, L.H.S. Lau, The long-term risk of metachronous advanced adenoma recurrence after endoscopic submucosal dissection for colorectal neoplasia: a propensity-score matched longitudinal cohort with 5-year follow-up, United European Gastroenterol J 13 (2025) 210–219.
[4] A. Rahimi, Z. Baghernejadan, A. Hazrati, K. Malekpour, L.N. Samimi, A. Najafi, R. Falak, H. Khorramdelazad, Combination therapy with immune checkpoint inhibitors in colorectal cancer: Challenges, resistance mechanisms, and the role of microbiota, Biomed. Pharmacother. 186 (2025) 118014.
[5] S. Li, T. Liu, C. Li, Z. Zhang, J. Zhang, D. Sun, Overcoming immunotherapy resistance in colorectal cancer through nano-selenium probiotic complexes and IL-32 modulation, Biomaterials 320 (2025) 123233.
[6] Q. Shen, J. Liu, L. Zeng, Y. Ren, J. Liao, S. Chen, Y. Tang, Z. Zhang, M. Jiang, H. Liao, L. Wang, X. Xu, J. Chen, Pancreas-targeted lipid nanoparticles for relatively non-invasive interleukin-12 mRNA therapy in orthotopic pancreatic ductal adenocarcinoma, J. Control. Release 381 (2025) 113588.
[7] Z. Hu, J. Shan, X. Jin, W. Sun, L. Cheng, X.L. Chen, X. Wang, Nanoarchitectonics of in situ antibiotic-releasing acicular nanozymes for targeting and inducing cuproptosis-like death to eliminate drug-resistant bacteria, ACS Nano 18 (2024) 24327–24349.
[8] C. Xiang, Q. Ding, T. Jiang, Y. Liu, C. Li, X. Yang, J. Jia, J. Xiang, Y. Wang, H. Zhou, Z. Lu, P. Gong, J.S. Kim, Reprogrammed glycolysis-induced augmentation of NIR-II excited photodynamic/photothermal therapy, Biomaterials 320 (2025) 123235.
[9] D.S. Ryu, H. Lee, S.J. Eo, J.W. Kim, Y. Kim, S. Kang, J.H. Noh, S. Lee, J.H. Park, K. Na, D.H. Kim, Photo-responsive self-expanding catheter with photosensitizer-integrated silicone-covered membrane for minimally invasive local therapy in malignant esophageal cancer, Biomaterials 320 (2025) 123265.
[10] C. Sun, Q. He, X. Yang, J. Wang, D. Xia, T. Xia, H. Liao, X. Xiong, Y. Liao, H. Shen, Q. Sun, Y. Yuan, Y. He, L. Liu, A novel NIR-dependent IDO-inhibiting ethosomes treatment melanoma through PTT/PDT/immunotherapy synergy, Colloids Surf. B: Biointerfaces 251 (2025) 114565.
[11] D. Feng, X. Kang, H. Wang, Z. He, H. Xu, Y. Li, A. Fan, H. Xu, Y. Zhang, J. Song, J. Hou, J. Qi, W. Zhang, Photochemical bomb: Precision nuclear targeting to activate cGAS-STING pathway for enhanced bladder cancer immunotherapy, Biomaterials 318 (2025) 123126.
[12] Q. Ren, T. Tian, B. Wang, J. Pan, Y. Huang, L. Zhong, Y. Wang, X. Wang, X. Huang, UVA-responsive Fe_3O_4@ZnO nanocarrier grafted with anti-EGFR antibody for precision delivery of Nrf2-siRNA and brusatol: a novel platform for integrated photodynamic, gene, and chemotherapy, Int. J. Biol. Macromol. 305 (2025) 141153.
[13] C. Yang, X. Liao, K. Zhou, Y. Yao, X. He, W. Zhong, D. Zheng, Y. Yang, M. Li, M. Zhou, Y. Zhou, L. Li, Y. Bai, K. Shi, Z. Qian, Multifunctional nanoparticles and collagenase dual loaded thermosensitive hydrogel system for enhanced tumor-penetration, reversed immune suppression and photodynamic-immunotherapy, Bioact. Mater. 48 (2025) 1–17.
[14] Y. Yang, Q. Zeng, C. Zhao, J. Shi, W. Wang, Y. Liang, C. Li, Q. Guan, B. Chen, W. Li, Metal-free antioxidant nanozyme incorporating bioactive hydrogel as an antioxidant scaffold for accelerating bone reconstruction, Biomaterials 320 (2025) 123285.
[15] B. Cui, S. Jiang, Y. Zhang, Y. Su, H. Zhou, H. Pang, MOF-based nanomaterials for advanced aqueous-ion batteries, Adv. Colloid Interf. Sci. 340 (2025) 103469.
[16] T. Luo, H.S. Jeppesen, A. Schoekel, N. Bönisch, F. Xu, R. Zhuang, Q. Huang, I. Senkovska, V. Bon, T. Heine, A. Kuc, S. Kaskel, Photocatalytic dehalogenation of aryl halides mediated by the flexible metal-organic framework MIL-53(Cr), Angew. Chem. Int. Ed. Eng. 64 (2025) e202422776.
[17] Y. Qian, C. Wang, R. Xu, J. Wang, Q. Chen, Z. Zhu, Q. Hu, Q. Shen, J.W. Shen, Copper-based metal-organic frameworks for antitumor application, J. Nanobiotechnol. 23 (2025) 135.
[18] W. Chen, X. Li, X. Wei, G. Liao, J. Wang, L. Li, Activation of peroxymonosulfate for degrading ibuprofen via single atom Cu anchored by carbon skeleton and chlorine atom: the radical and non-radical pathways, Sci. Total Environ. 858 (2023) 160097.
[19] G. Ashraf, M. Asif, A. Aziz, T. Iftikhar, Z.T. Zhong, S. Zhang, B. Liu, W. Chen, Y. D. Zhao, Advancing interfacial properties of carbon cloth via anodic-induced self-assembly of MOFs film integrated with α-MnO(2): a sustainable electrocatalyst sensing acetylcholine, J. Hazard. Mater. 426 (2022) 128133.
[20] X. Liu, L. Mei, J. Wang, X. Liu, Y. Yang, Z. Wu, Y. Ji, Cutting-edge insights into the mechanistic understanding of plant-derived exosome-like nanoparticles: Implications for intestinal homeostasis, Food Res. Int. 208 (2025) 116186.
[21] M.C. Manzaneque-López, A. González-Arce, P. Pérez-Bermúdez, C. Soler, A. Marcilla, C.M. Sánchez-López, Pasteurization and lyophilization affect membrane proteins of pomegranate-derived nanovesicles reducing their functional properties and cellular uptake, Food Chem. 483 (2025) 144303.
[22] J. Kim, Y. Zhu, S. Chen, D. Wang, S. Zhang, J. Xia, S. Li, Q. Qiu, H. Lee, J. Wang, Anti-glioma effect of ginseng-derived exosomes-like nanoparticles by active blood-brain-barrier penetration and tumor microenvironment modulation, J. Nanobiotechnol. 21 (2023) 253.
[23] X. Wang, R. Tian, C. Liang, Y. Jia, L. Zhao, Q. Xie, F. Huang, H. Yuan, Biomimetic nanoplatform with microbiome modulation and antioxidant functions ameliorating insulin resistance and pancreatic β-cell dysfunction for T2DM management, Biomaterials 313 (2025) 122804.
[24] W. Feng, Y. Teng, Q. Zhong, Y. Zhang, J. Zhang, P. Zhao, G. Chen, C. Wang, X. J. Liang, C. Ou, Biomimetic grapefruit-derived extracellular vesicles for safe and targeted delivery of sodium thiosulfate against vascular calcification, ACS Nano 17 (2023) 24773–24789.
[25] Y. Chen, Z. Qin, Y. Wang, B. Gu, J. Wang, Y. Zheng, Y. Niu, L. Jia, CD44-targeted virus-mimicking nanomedicine eliminates cancer stem cells and mitigates chemoresistance in head and neck squamous cell carcinoma, Mater. Today Bio 32 (2025) 101721.
[26] S. Zhang, W. Hu, Y. Zhao, Y. Liao, K. Zha, W. Zhang, C. Yu, J. Liao, H. Li, W. Zhou, F. Cao, B. Mi, G. Liu, Bidirectional modulation of glycolysis using a multifunctional

nanocomposite hydrogel promotes bone fracture healing in type 2 diabetes mellitus, Bioact. Mater. 50 (2025) 152–170.
[27] Y. Fang, F. Hu, W. Ren, L. Xiang, T. Wang, C. Zhu, R. He, X. Dong, C. Liu, H. Ding, K. Zhang, Nanomedicine-unlocked radiofrequency dynamic therapy dampens incomplete radiofrequency ablation-arised immunosuppression to suppress cancer relapse, Biomaterials 317 (2025) 123087.
[28] S. Zhang, J. Li, X. Hu, Z. Chen, J. Dong, C. Hu, S. Chao, Y. Lv, Y. Pei, Z. Pei, H2S and NIR light-driven nanomotors induce disulfidptosis for targeted anticancer therapy by enhancing disruption of tumor metabolic symbiosis, Chin. Chem. Lett. 36 (2025) 110314.
[29] S. Sharafinia, N.S. Ardestani, A. Rashidi, F. Abbasy, P. Eskandari Sabzi, CO(2)/N(2) selectivity with high efficiency using new flexible coordinate organic polymer-based core-shell, RSC Adv. 15 (2025) 29284–29299.
[30] A.A. Santos, C.N. Keim, V.F. Magalhães, A.B.F. Pacheco, Microcystin drives the composition of small-sized bacterioplankton communities from a coastal lagoon, Environ. Sci. Pollut. Res. Int. 29 (2022) 33411–33426.
[31] E.A. Demirci, S. Önder, T. Acar, S.Z. Sunar, G. Torun Köse, KR12 peptide-modified ECM coating for enhanced osteogenic and antimicrobial activity of titanium surfaces, Biomater. Adv. 179 (2026) 214515.
[32] Y. Li, N. Wang, J. Hu, M. Luo, N. Zhang, L. Gao, The mechanism of plasma exosome miR-15a-5p targeting the CF-modified protein IGF1R to regulate alveolar epithelial autophagy and influence pulmonary interstitial fibrosis, Non-coding RNA Res. 15 (2025) 51–64.
[33] J. Lanka, S. Kumar, M.K. B, S. Rao, S. Gadag, U.Y. Nayak, Drug release and cytotoxicity of Hyaluronic acid and Zinc oxide gels, an in-vitro study, Des. Monomers Polym. 25 (2022) 212–219.
[34] S. Rahamouz-Haghighi, M. Akaberi, S.A. Emami, Z. Tayarani-Najaran, Biochemical profiling and protective effects of Scutellaria litwinowii against AlCl(3)-Induced neurotoxicity in PC12 cells, J. Ethnopharmacol. 354 (2026) 120504.
[35] A.L. Liu, H. Lv, H.Y. Wang, H. Yang, Y. Li, Y.F. Jia, J.M. Qian, Probiotics reduce the severity of DSS-induced colitis in aged mice by enhancing intestinal barrier function and modulating gut microbiota, GeroScience (2025), https://doi.org/10.1007/s11357-025-01900-6IF.
[36] Y. Wang, Z. Chen, J. Li, Y. Wen, J. Li, Y. Lv, Z. Pei, Y. Pei, A paramagnetic metal-organic framework enhances mild magnetic hyperthermia therapy by downregulating heat shock proteins and promoting ferroptosis via aggravation of two-way regulated redox dyshomeostasis, Adv. Sci. Weinh. Baden-Wurtt. Ger. 11 (2024) e2306178.
[37] P. Wang, H. Liu, L. Guo, Y. Tang, T. Lan, R. Zhou, H. Xu, L. Wang, X. Wang, B. Chen, Y. Wang, S. Wang, C. Liu, J. Chen, C. Xu, Q. Wang, H. Tian, MIL-100(Fe)-based Co-delivery platform as cascade synergistic chemotherapy and immunotherapy agents for colorectal cancer via the cGAS-STING pathway, Acta Biomater. 204 (2025) 582–595.
[38] W. Jin, Z. Chen, Y. Wang, J. Li, J. Li, Y. Pei, Z. Pei, Nano metal-photosensitizer based on Aza-BODIPY-Cu complex for CDT-enhanced dual phototherapy, Chin. Chem. Lett. 35 (2024) 109328.
[39] J. Li, B. Hu, Z. Chen, J. Li, W. Jin, Y. Wang, Y. Wan, Y. Lv, Y. Pei, H. Liu, Z. Pei, Mn (iii)-mediated carbon-centered radicals generate an enhanced immunotherapeutic effect, Chem. Sci. 15 (2024) 765–777.